International Journal of Hydrogen Energy 251 (2026) 156005

Contents lists available at ScienceDirect

International Journal of Hydrogen Energy

journal homepage: www.elsevier.com/locate/he

CFD modeling of an experimental protonic membrane steam methane reformer

Yifei Wang [a], Dominic Peters [a], Xiaodong Cui [a], Henrik Wang [a], Feiyang Ou [a], Carlos G. Morales-Guio [a,*], Panagiotis D. Christofides [a,b,*]

[a] Department of Chemical and Biomolecular Engineering, University of California, Los Angeles, CA, 90095-1592, USA
[b] Department of Electrical and Computer Engineering, University of California, Los Angeles, CA 90095-1592, USA

ARTICLE INFO

Keywords:
Protonic membrane reformer (PMR)
Steam methane reforming
Computational fluid dynamics (CFD) modeling
Model validation
Process analysis
Process optimization

ABSTRACT

Conventional steam methane reforming systems suffer from costly downstream purification steps. Protonic membrane reformers offer a promising alternative by integrating thermal and electrochemical catalysis into a single reactor-separator unit to generate high-purity hydrogen. In this work, a two-dimensional axisymmetric computational fluid dynamics model was developed in ANSYS Fluent and parameterized using an experimental Ni-$BaZr_{0.8-x}Ce_xY_yO_{3-\delta}$ protonic membrane reformer. To expand on previous CFD studies of similar thermo-electrochemical reformers, this work simulates a novel flow field model for a tube-in-tube reformer geometry that resolves coupled mass and energy transport between the feed tube and anode chamber control volumes. The results of the CFD model demonstrate that hydrogen separation at a current density 0.59 A cm^{-2} shifts the thermodynamic equilibrium of the SMR reaction toward higher methane conversion (99.9%) and increases hydrogen production (67.6 Nml min^{-1}). Stagnant flow fields within the tube-in-tube reformer are also identified, revealing transport limitations that affect methane conversion.

1. Introduction

Hydrogen has attracted significant research interest due to its use in the chemical industry, and its potential as an energy carrier or fuel alternative for the transportation and industrial sectors [1]. Beyond energy applications, hydrogen is also an essential feedstock in the production of chemicals such as methanol, ammonia, fertilizers, petrochemicals, and iron ore [2,3]. These diverse applications underscore hydrogen's critical role in facilitating energy availability and enabling energy transfer across economic sectors. As of 2023, steam methane reforming and coal gasification were the primary methods for hydrogen production worldwide, accounting for approximately 90% of total production [4].

In previous studies, we designed, fabricated, and automated a Joule-heated SMR system to enable precise temperature control over a wash-coated tubular reformer [5]. However, electrified SMR produces a hydrogen stream that also contains by-products, which requires downstream separation operations, increasing the cost of electrified SMR process designs [6]. Alternatively, hydrogen separation membranes have gained attention for their ability to separate hydrogen directly from the reformer, thereby enhancing hydrogen productivity and isolating by-products. Conventional metallic membranes, typically composed of Pd or Pd–Ag alloys, achieve separation through a pressure differential across the membrane reformer unit [7]. Although effective, these pressure-driven systems require additional hydrogen compression, increasing process complexity and energy consumption compared to state-of-the-art electrochemical membrane reformers.

Protonic membrane reformers (PMR) integrate hydrogen production and separation within a single processing unit. In generating a pressurized, high-purity hydrogen stream, the PMR eliminates the need for additional product separations. Such a design does not require an external combustion furnace or pressure-swing adsorption beds, allowing for a compact system architecture and reduced emissions. Malerød-Fjeld, et al. [8] tested a lab-scale PMR unit that selectively extracted hydrogen at 0.4 A cm^{-2}. The concurrent Joule heating of the protonic membrane under the applied current density was shown to deliver additional thermal energy to the PMR reaction zone. The authors reported near-zero thermodynamic energy losses and complete methane conversion, promising a path for future modular hydrogen platforms that incorporate thermo-electrochemical membrane technologies.

In chemical engineering literature, CFD simulations have been widely used for the analysis of SMR systems that utilize hydrogen separation membranes [9–11]. Specifically, [12] employed COMSOL

* Corresponding authors.
E-mail addresses: moralesguio@ucla.edu (C.G. Morales-Guio), pdc@seas.ucla.edu (P.D. Christofides).

https://doi.org/10.1016/j.ijhydene.2026.156005
Received 23 March 2026; Received in revised form 12 May 2026; Accepted 9 June 2026
Available online 22 June 2026

software to investigate a 2D axisymmetric catalytic membrane reactor with a Pd-Ru metallic membrane and Ni-Al_2O_3 catalyst for hydrogen production from natural gas. The model examines the effects of operating temperature, gas hourly space velocity, and sweep gas flow on methane conversion and hydrogen permeation. The results indicate 99.9% methane conversion at 1000 K and significant hydrogen separation, highlighting the potential for efficient hydrogen production. In another study conducted by [13], catalytic membrane reactors and baffled membrane reactors were compared using ANSYS Fluent simulations, showing that baffles in the reformer unit reduce concentration and thermal gradients and improve flow uniformity, with better stability at higher gas hourly space velocities. An analogous study conducted by [14] was also reported, in which ANSYS Fluent was used to investigate a membrane-integrated reformer. These results demonstrated that higher steam-to-carbon ratios and optimal sweep conditions improve methane conversion and hydrogen recovery, while flow direction, pressure, and membrane length significantly influence performance, highlighting the benefits of metallic membrane integration.

While numerous studies have focused on CFD simulations for steam methane reforming, research targeting the multi-physics of solid oxide PMRs is still comparatively sparse and only recently gaining momentum. Existing PMR modeling efforts are often based on literature-reported reactor descriptions and are validated primarily against literature data [15], rather than being developed and validated for a specific, laboratory-built experimental reactor. Motivated by this, the present work develops a CFD model based on the actual configuration of an experimental PMR unit, in which a single $BaZr_{0.8-x}Ce_xY_yO_{3-\delta}$ protonic membrane reformer was integrated into a watt-scale SMR process. Unlike previous PMR modeling studies that typically consider single-pass tubular geometries, the modeled reformer geometry uses a new tube-in-tube approach to preheat the feed gas in a heat-exchange feed tube. The developed geometry-specific model is validated with experimental data to provide realistic representations of the steady-state reformer operability at various operating points. This model was developed to parametrize and optimize the designs of PMRs and to highlight the critical process and design variables that maximize hydrogen production.

Generally, the simulation enables a 2D analysis of the hydrogen flux through the protonic membrane, and the impact that the hydrogen extraction rate has on both hydrogen production and methane conversion. In this respect, the model focuses primarily on the thermo-electrochemical reactions that occur at the anode surface, where methane conversion, hydrogen generation, and hydrogen extraction occur. The experimental PMR system and measurement methods are first described in Section 3, followed by the CAD modeling and mesh characterization of the modeled reformer geometry in Section 4. The numerical methods used for the CFD implementation are then presented in Section 5, along with the transport and governing equations that define the multi-physics model in Section 6. Validation against measurements of temperature and gas composition in the experimental PMR confirms the model accuracy and allows for the reproduction of key reactor multi-physics in the user-defined computational domain. The results and analysis of the 2D axisymmetric CFD model, including comparisons with measurements and a parametric study evaluating the influence of applied current on hydrogen recovery, are presented in Section 7. This is a first step toward further development of optimized PMRs that can scale in function and size, and recommendations are provided in Section 8.

2. Preliminaries

Definitions of variables used in the modeling of the reactor:

- A_i: Pre-exponential factor of adsorption constant K_i [Pa^{-1} for $i = CH_4, H_2, CO$; unitless for $i = H_2O$].
- A_j: Pre-exponential factor of rate coefficient k_j [mol $Pa^{0.5}$ kg_{cat}^{-1} s^{-1} for $j = 1$ (SMR); mol Pa^{-1} kg_{cat}^{-1} s^{-1} for $j = 2$ (WGS)].
- c_v, c_p, $c_{p,i}$: Specific heat capacity at constant volume of the mixture, and specific heat capacity at constant pressure of the mixture and species i, respectively [J kg^{-1} K^{-1}].
- C_i: Concentration of species i [mol m^{-3}].
- D_{ij}: Binary diffusion coefficient [m^2 s^{-1}].
- E_{fluid}, E_{solid}: Total specific energy of the fluid and solid, respectively [J kg^{-1}].
- E_j : Activation energy of thermal reaction j [J mol^{-1}]
- $F_{H_2,ex}$: Extraction rate of hydrogen gas [mol s^{-1}].
- $\vec{g}$: Gravitational acceleration [m s^{-2}].
- H_{fluid}, H_{solid}: Specific enthalpy of the fluid and solid, respectively. [J kg^{-1}].
- k_i: Thermal conductivity of species i [W m^{-1} K^{-1}].
- $k_{r,j}$: Reaction rate constant of thermal reaction j [mol $Pa^{0.5}$ kg_{cat}^{-1} s^{-1} for $j = 1$ (SMR); mol Pa^{-1} kg_{cat}^{-1} s^{-1} for $j = 2$ (WGS)].
- K_i: Adsorption constant of species i [Pa^{-1} for $i = CH_4, H_2, CO$; unitless for $i = H_2O$].
- K_j: Equilibrium constant of thermal reaction j [Pa^2 for $j = 1$ (SMR); unitless for $j = 2$ (WGS)].
- P, P_i: System pressure and partial pressure of species i, respectively [Pa].
- r_1, r_2: SMR reaction rate and WGS reaction rate, respectively. [mol kg_{cat}^{-1} s^{-1}].
- R: Universal gas constant [J mol^{-1} K^{-1}].
- T: Temperature [K].
- T_{feed}: Anodic feed gas temperature [K].
- U_{fluid}: Specific internal energy of the fluid [J kg^{-1}].
- u: Velocity magnitude [m s^{-1}].
- $\vec{v}$: Velocity vector [m s^{-1}].
- W_{cat}: Effective catalyst weight [kg].
- $X_{i,j}$: Mole fraction of species i, j [–].
- $Y_{i,j}$: Mass fraction of species i, j [–].
- ρ: Density [kg m^{-3}].
- $\dot{m}_{in}$: Anodic feed mass flow rate [kg s^{-1}].

3. Experimental PMR system and digitalization

3.1. Overview

All experimental measurements used for the CFD modeling of a protonic membrane reformer were conducted using a watt-scale experimental steam methane reforming system. The system is comprised of the following physical and chemical processing units: a 15.2 cm^2 protonic membrane (CoorsTek, Inc.), an electric furnace (Thermolyne® 21,100 Tube Furnace), two steam bubblers, and two condensers. Fig. 1 shows the experimental PMR system with the aforementioned processing units and instrumentation. An array of sensors is also integrated in the experimental system to allow for real-time measurements of key process parameters. The key sensors of the PMR process are: four mass flow controllers (Brooks Instrument SLA5850 Series), two bubbler pressure transducers and thermocouples (DwyerOmega PX359-1KGI transducers; DwyerOmega, OD: 1/16 inch thermocouple probes), two pressure transducers for the anode and cathode chambers, an anode chamber thermocouple, two back pressure regulators (Equilibar LF-Series) for the anodic and cathodic streams, a gas chromatograph (Agilent 7890B Gas Chromatograph) downstream of the anodic condenser, and an outlet digital flow meter (Alicat M Series) placed downstream of the cathodic condenser. The complete P&ID of the experimental setup was previously reported in [16].

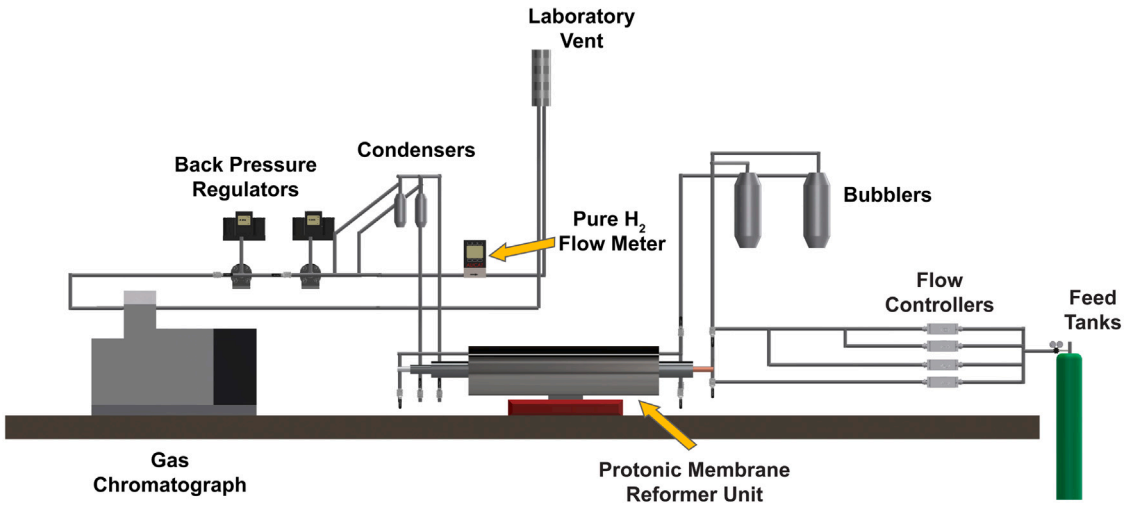

Fig. 1. Schematic of the experimental PMR unit.

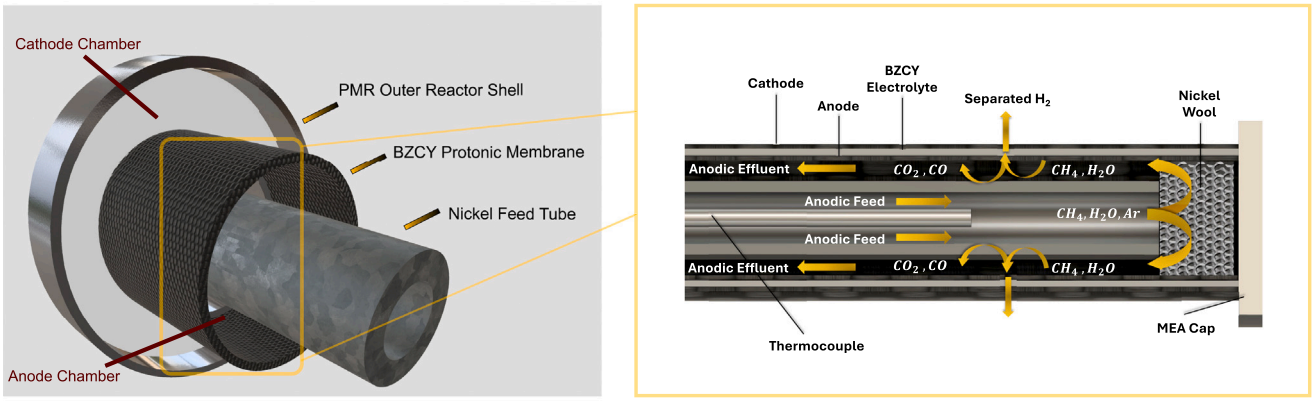

Fig. 2. Schematic of the thermo-electrochemical processes within the PMR unit.

3.2. Experimental protonic membrane reformer

The experimental protonic membrane reformer is made from a doped barium-zirconate ceramic that selectively separates hydrogen from product streams over an active anode surface area of 15.2 cm^2. Both the anode and cathode electrodes of the PMR unit were created from dip-coated slurries of Ni particles (60 wt%) and BZCY ceramic powders [8]. Fig. 2 depicts the internal configuration of the PMR unit, which is the core of the PMR system. In the experimental setup, a nickel feed tube delivers a reactant gas mixture into the furthest point of the anode chamber, and a thermocouple is positioned near the far end of the anode chamber to provide direct measurements of internal gas temperatures. Nickel wool is also packed into the end of the nickel feed tube that functions as the current collector for the anode side (inner side) of the tubular membrane electrode assembly (MEA). When an external current is applied to the electrochemical circuit, the electrochemical oxidation of hydrogen to protons occurs at the anode, the generated protons migrate through the solid BZCY electrolyte, and the electrochemical reduction of these protons to hydrogen occurs at the cathode. As a result, the protonic membrane reformer is able to convert methane into typical SMR products on the anode, hydrogen and carbon oxides, while simultaneously separating and compressing the hydrogen target product on the cathode. With this technology, operation at current densities greater than 0.59 A cm^2 is possible [17].

3.3. Process digitalization

All mass flow controllers were connected to a LabVIEW user interface via RS-232 communications, enabling read and write privileges to sensors and actuators on a per-second basis. Each bubbler unit of the test bed was heated by electrical heating tapes (BriskHeat Insulated Heat Tape) connected to power supplies (Omega CS8DPT Universal Benchtop Controller) operating under PD closed-loop control to regulate steam temperatures. The control input was the voltage supplied to the heating tapes, and the control output was the temperature of each bubbler. The electric potential supplied to the PMR unit was actuated with a potentiostat (Metrohm PGSTAT302N and 20 A Booster) controlled from the LabVIEW user interface. The temperature and pressure readings for the PMR feeds and bubbler units were integrated into LabVIEW through a CompactRIO data acquisition device for programmable and automatic feedback control. An automation algorithm was developed to process the anode effluent peak areas from GC signal files every 18 min. To quantify the pure hydrogen outlet stream, RS-232 communications were used to transmit per-second volumetric flow rate readings from the digital outlet flow meter. The established digital communication architecture allowed for synchronized sensing, process control, and automation of the PMR system and for data generation spanning the feasible operating region (0.0–0.6 A cm^{-2}; 10–30 Nml min^{-1} of CH_4; 120–130 °C bubbler temp.).

Table 1
Geometric dimensions of the experimental protonic membrane reformer.

Dimension	Value (mm)
Protonic membrane length	60.9
Protonic membrane O.D.	9.00
Protonic membrane I.D.	7.00
Nickel feed tube length	5.20
Nickel feed tube O.D.	4.50
Nickel feed tube I.D.	3.15

3.4. Steady-state experimental design

The nominal operating point of the system was set at a current density of 0.0 A cm^{-2}, a methane feed flow rate of 16.2 Nml min^{-1}, and an initial reformer temperature of 737 °C. Two additional steady-state measurements were taken at 0.30 and 0.59 A cm^{-2} to validate the CFD model at multiple hydrogen extraction rates. The steam-to-carbon ratio and cathode chamber pressure were 3.3 and 3.15 bar, respectively, for all steady-state experiments. To extract kinetic parameters, parametric studies for temperature and pressure were performed on the PMR at system pressures of 1.0 bar and 3.2 bar at 0.0 A cm^{-2}. For the kinetic experiments at the nominal operating points, five GC measurements were taken per steady state over a temperature range of 584 to 786 °C. This procedure was repeated three times, and for each steady-state run, the PMR anode and cathode catalysts were reduced under pure hydrogen streams at 800 °C for five hours, prior to the start of each experiment. These results were used to validate the lumped-parameter reactor model developed in [18], which enabled the calculation of the nickel loading on a catalytic washcoat. The same method was used in this CFD study to approximate nickel loading on the electrode surfaces of the experimental protonic membrane. After validating the catalyst loading parameter against experimental, kinetically-limited steady-state data, two additional steady-state measurements were obtained at 3.2 bar under applied current densities of 0.30 and 0.59 A cm^{-2}, resulting in internal reformer temperatures of 760 and 820 °C, respectively.

4. CAD model and mesh development

A 2D computer-aided design (CAD) model was developed from the dimensions of the experimental PMR, as discussed in the last section. These dimensions are provided in Table 1, and several simplifications were made when constructing the CFD computational domain to minimize computational complexity of the model. The CAD considers only the inner region of the anode chamber, which does not include the solid outer reactor wall or the cathode. Additionally, the catalyst layer on the anode surface is thin compared to the overall anode chamber geometry of the PMR, and thus it is assumed to have a negligible impact on bulk gas flow [8]. The effect of the catalyst layer on reaction kinetics, however, is accounted for via an effective catalyst weight included in the reaction kinetics equations. The thickness of the outside layers of the membrane, such as the outer reactor shell and furnace are also neglected in the CFD model, as its primary effect on the SMR reaction kinetics is limited to heat transfer from the external heating source, and the temperature distribution in the axial direction cannot be accurately measured in the experiment, making it difficult to define precise thermal boundary conditions at the anode surface. Instead, the thermal effect of the external heating source is represented by a constant heat flux applied to the anode surface as a boundary condition, as will be discussed in detail below. This approximation is justified as the length of the tubular electric furnace is at least five times longer than that of the PMR, and the PMR is located near the center of the furnace.

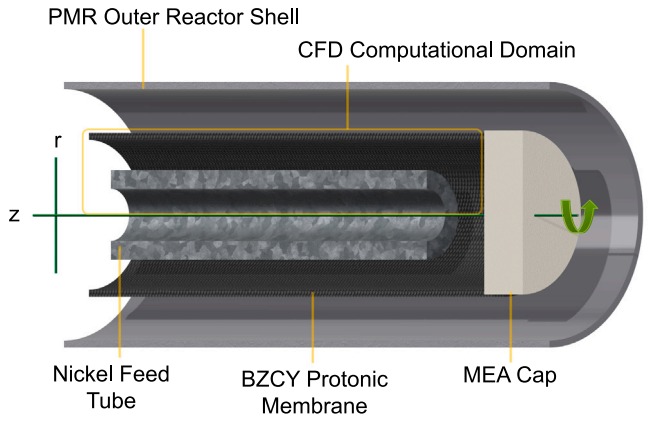

Fig. 3. Simplified cylindrical schematic of the PMR reactor (not drawn to scale). The nickel feed tube delivers the reactant gas mixture to the inlet of the anode chamber that is housed within the BZCY protonic membrane. The PMR reactor shell houses the cathode chamber. The anode surface along the inner wall of the protonic membrane facilitates hydrogen oxidation. The cathode surface along the outer wall of the protonic membrane induces hydrogen reduction. The yellow box highlights the computational domain for the developed CFD model that spans horizontally from $z = 0.00$ m to $z = 6.10 \times 10^{-2}$ m and radially from $r = 0.00$ m to $r = 3.50 \times 10^{-3}$ m.

The assumption of axial symmetry for the PMR model is physicochemically justified by the specific dimensionless regimes and experimental configuration of the system. Though 3D features can emerge in larger systems, the following physical arguments support a 2D modeling approach for this laboratory-scale reactor. First, in the laminar regime in which our reactor operates (Reynolds number of 7), viscous forces dominate over inertial forces, precluding the formation of 3D instabilities, swirls, or asymmetric flow patterns. Furthermore, given the inlet tube is sufficiently long to ensure that the velocity profile is fully developed before reaching the catalytic reaction zone, a symmetric flow field is established. Second, transport rates are an order of magnitude larger than kinetic rates in this reformer geometry at the specified operating conditions. In other words, molecular diffusion is an order of magnitude faster than the kinetic rates of the SMR and WGS reactions. This creates a "smoothing effect" in which any potential circumferential concentration gradients are equilibrated almost instantaneously by diffusion. This high rate of transport relative to the reaction kinetics ensures a uniform species distribution around this axis, making the 2D radial-axial modeling framework a scientifically reasonable and accurate representation of PMR physics. Therefore, a 2D axisymmetric model is sufficient to capture the essential fluid transport and reaction phenomena occurring in both the axial and radial directions of the PMR. The validity of this 2D approach has also been confirmed by laboratory-scale experimental data. The added complexity of a 3D model would provide negligible improvements to the accuracy of the flow profiles or reaction analysis, while significantly increasing computational overhead.

A simplified PMR geometry is shown in Fig. 3, where the anode chamber of the PMR is treated as a cylindrical reactor, and the rectangular area marked by the yellow box is defined as the computational domain using the 2D axisymmetric model. In the 2D computational domain, the anodic feed gas mixture, which is comprised of methane, steam, hydrogen, and argon, is introduced through the gas inlet located on the bottom half of the left boundary. The gas travels to the right, axially, through the annular gap between the feed tube wall and the catalyst surface, reaches the MEA cap (right boundary), reverses direction, and exits through the annular space toward the anode chamber outlet. Considering the highly axisymmetric architecture of the reformer, the angular information in the PMR is redundant and a 3D model is not needed.

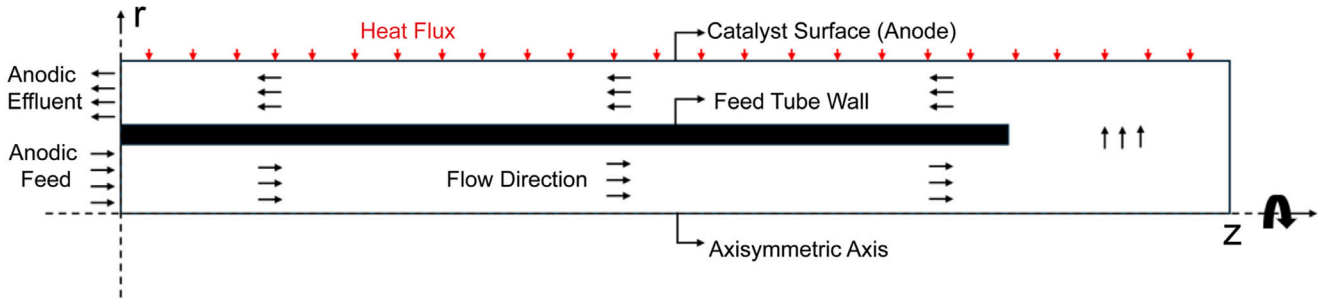

(a) 2D axisymmetric computational domain, including the gas inlet, gas outlet, catalyst surface embedded within the membrane wall, reactor cap (right boundary), and the axisymmetric axis.

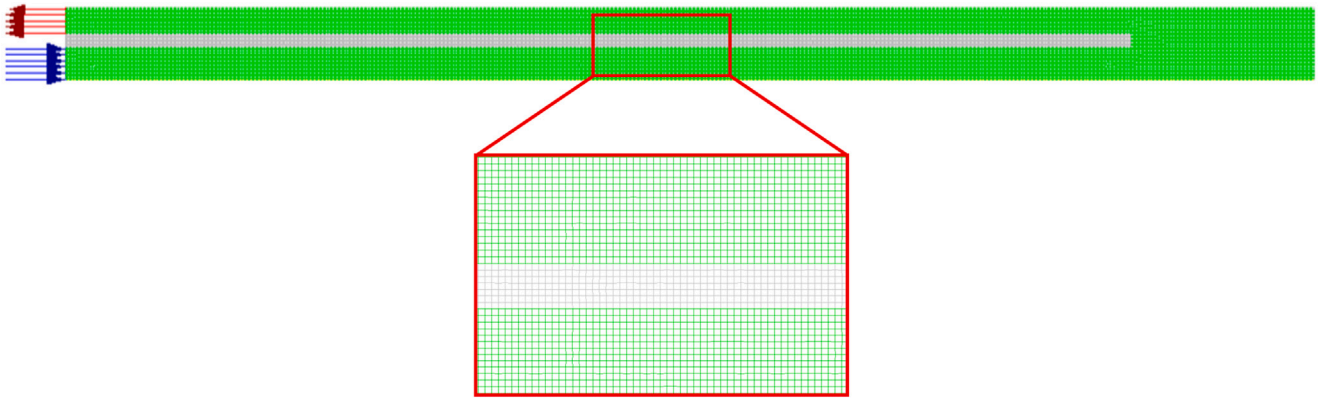

(b) Computational mesh of the simulation domain, showing both the overall mesh structure and a magnified view of a selected mesh region.

Fig. 4. Computational domain and mesh used in the simulation. (a) Domain geometry. (b) Mesh structure.

In the CFD simulation, the computational domain is discretized into smaller subdomains, known as grids, that collectively form the computational mesh. Within each grid, spatial variations are minimized throughout the entire domain, allowing for localized approximation of relevant phenomena. Specifically, each discretized grid forms the PMR mesh used to solve the continuity equation, momentum equations, and transport equations in each subdomain. The locally computed solutions are then integrated, allowing for the reconstruction of the overall fluid flow and temperature fields across the entire domain. The reliability of the CFD simulation results is highly dependent on the mesh metrics, such as orthogonality, skewness, and aspect ratio. In general, the computational mesh quality is carefully optimized to ensure a balance between computational efficiency and sufficient spatial resolution to accurately capture the physical phenomena of interest. A poorly constructed mesh can lead to poor accuracy of the solution, whereas an excessively refined mesh, while enhancing solution precision, significantly increases computational cost. Thus, a balance between computation efficiency and necessary resolution is critical to capture the essential physical phenomena in the CFD simulation when designing the mesh.

In the simulation, a quadrilateral-dominant mesh of 2.2×10^5 cells, with a characteristic cell size of 0.1 mm, is utilized. The use of quadrilateral elements ensures solution accuracy in well-defined regions, while the automatically generated triangular elements provide flexibility in areas with intricate geometries. All relevant mesh metrics are shown in Table 2, and the computational mesh is illustrated in Fig. 4. With an average element quality of 0.99, the mesh elements are nearly ideal in shape, ensuring high numerical accuracy. The average aspect ratio of 1.01 shows that the elements are almost uniform, minimizing errors in the solution. With an average skewness of 4.49×10^{-3}, the mesh exhibits minimal distortion, further improving the reliability of the solution. Finally, the average orthogonal quality of 0.99 confirms that the mesh faces are nearly perpendicular, which is critical for accurate gradient calculations and numerical stability in cylindrical coordinates. A mesh independence study showed that the selected mesh settings are sufficient for accurate simulation results and computational efficiency. Further refinement of the mesh, while increasing computational cost, yielded results nearly identical to those obtained with the studied mesh configuration.

Table 2
Mesh quality evaluation for the computational domain.

Mesh Metric	Value
Average element quality	0.99
Average aspect ratio	1.01
Average skewness	0.01
Average orthogonal quality	0.99

Remark 1. With the second Damköhler number on the order of 10^{-1}, the flux of reactant to the anode is not diffusion-limited, and the intrinsic kinetics of the SMR and WGS drive the overall rates of reaction. This further reduces the necessity of explicitly modeling solid-phase catalyst particles or catalyst layers in the multi-physics simulation. Simulations at higher temperatures and current densities than those tested here would eventually be transport-limited; however, those operating conditions are avoided, as they are detrimental to the PMR.

5. Numerical modeling approach

5.1. Chemical reaction kinetics model

To simulate the thermal chemical reactions that occur within the anode chamber of the PMR, a kinetic model was developed that

describes reaction rates as a function of pressure, temperature, and feed flow rates. On the microscopic scale, the PMR reactant mixture flows through a convective bulk fluid and diffuses toward the catalytic surface of the anode. The reaction products then diffuse from these catalyst sites back to the anode surface, re-enter the bulk fluid, and are eventually transported by convection to the reformer outlet [19]. However, it is unnecessary to employ a detailed kinetic model that explicitly accounts for all microscopic phenomena occurring around the nickel catalyst layer of the anode, as this would significantly increase model complexity and solution time. Therefore, a lumped-parameter macro-kinetic model developed by [20], based on the Langmuir–Hinshelwood–Hougen–Watson (LHHW) formalism, is utilized in this simulation to describe the macroscopic reaction rates of both the SMR and WGS reactions. Although the detailed transport phenomena within the catalyst layer are not explicitly resolved, the impact of the number of available surface sites on anodic production rates is accounted for by incorporating an effective catalyst weight in the LHHW kinetic model, which will be discussed in detail later. The governing rate expressions are given in the following equations.

Specifically, the reaction rates of the SMR and WGS are given by the following macroscopic kinetic equations:

$$CH_4 + H_2O \rightleftharpoons CO + 3\,H_2, \qquad \Delta H^{\circ}_{298\,K} = +206\,\mathrm{kJ\,mol^{-1}} \tag{1a}$$

$$r_1 = \frac{k_1}{P_{H_2}^{2.5}}\left(P_{CH_4}P_{H_2O} - \frac{P_{H_2}^3 P_{CO}}{K_1}\right)/\mathrm{DEN}^2 \tag{1b}$$

$$CO + H_2O \rightleftharpoons CO_2 + H_2, \qquad \Delta H^{\circ}_{298\,K} = -41\,\mathrm{kJ\,mol^{-1}} \tag{2a}$$

$$r_2 = \frac{k_2}{P_{H_2}}\left(P_{CO}P_{H_2O} - \frac{P_{H_2}P_{CO_2}}{K_2}\right)/\mathrm{DEN}^2 \tag{2b}$$

$$\mathrm{DEN} = 1 + \frac{K_{H_2O}P_{H_2O}}{P_{H_2}} + K_{CO}P_{CO} + K_{H_2}P_{H_2} + K_{CH_4}P_{CH_4} \tag{3}$$

where P_{H_2}, P_{CH_4}, P_{H_2O}, P_{CO}, and P_{CO_2} represent the partial pressures of H_2, CH_4, H_2O, CO, and CO_2, respectively, on the anode surface, which can be determined based on Dalton's law and the ideal gas law:

$$P_i = C_i RT \tag{4}$$

The terms K_{H_2}, K_{CH_4}, and K_{CO} are the adsorption constants for H_2, CH_4, and CO, respectively, while K_{H_2O} is the dissociative adsorption constant for H_2O. The parameters k_1, k_2 are the rate coefficients for the SMR reactions and the WGS reactions, and DEN is a dimensionless parameter derived from the number of available active sites. The adsorption constants and dissociative adsorption constants can be determined based on:

$$\begin{aligned} k_{r,j} &= A_j \exp\left(-\frac{E_j}{RT}\right), \quad j = 1,2 \\ K_i &= A_i \exp\left(-\frac{\Delta H_i}{RT}\right), \quad i = CH_4, H_2O, CO, H_2 \end{aligned} \tag{5}$$

All kinetic parameters are summarized in Table 3. This chemical kinetics model is expressed in units of mol $kg^{-1}_{catalyst}$ s^{-1}, which establishes a catalyst-mass basis for the thermal reaction rates in the PMR.

The hydrogen extraction rate through the membrane, also referred to as hydrogen flux, is directly determined by the charge balance across the protonic membrane cell of the reformer unit, expressed as follows:

$$n_e F\, F_{H_2,ex} = \eta_F I \tag{6}$$

where n_e represents the number of electrons transferred per mole of extracted hydrogen, which is 2 e-/mol H_2 in this case, F is the Faraday constant, and $F_{H_2,ex}$ represents the molar extraction rate of hydrogen from the PMR membrane. The term η_F is the Faradaic efficiency, representing the fraction of the applied current that contributes to the hydrogen extraction rate, and I is the total applied current to the protonic membrane. For the present study, a Faradaic efficiency of 100% is assumed for the electrochemical hydrogen flux, based on our previous experimental observations [17]. Based on this assumption, Eq. (6) can be rearranged to give:

$$F_{H_2,ex} = \frac{I}{2F} \tag{7}$$

where the hydrogen extraction rate is directly proportional to the applied current. This expression is implemented as a uniformly distributed source term at the membrane wall to account for hydrogen extraction.

Table 3
Kinetic parameters from [20].

Parameter	Value	Unit
E_1	240.1	kJ mol^{-1}
E_2	67.13	kJ mol^{-1}
A_1	4.225×10^{15}	kmol $bar^{0.5}$ $(kg_{cat}\ hr)^{-1}$
A_2	1.955×10^{6}	kmol (kg bar $hr)^{-1}$
K_1	1.198×10^{13}	bar^2
K_2	1.767×10^{-2}	–
A_{CO}	8.23×10^{-5}	bar^{-1}
A_{H_2}	6.12×10^{-9}	bar^{-1}
A_{CH_4}	6.65×10^{-4}	bar^{-1}
A_{H_2O}	1.77×10^{5}	–
ΔH_{CO}	−70.65	kJ mol^{-1}
ΔH_{H_2}	−82.9	kJ mol^{-1}
ΔH_{CH_4}	−38.28	kJ mol^{-1}
ΔH_{H_2O}	88.68	kJ mol^{-1}
W_{cat}	4×10^{-4}	kg

Table 4
Gas species source terms in the CFD model.

Gas Species	Source Term
CH_4	$-r_1 W_{cat}$
H_2O	$(-r_1 - r_2) W_{cat}$
CO	$(r_1 - r_2) W_{cat}$
H_2 (reaction)	$(3r_1 + r_2) W_{cat}$
H_2 (membrane extraction)	$-\frac{I}{2F}$
CO_2	$r_2 W_{cat}$
Ar	0

The primary objective of these developed relations (Eqs. (1), (2), (3), (5), (6)) is to provide a physically consistent mapping between key process variables (temperature, partial pressures) and reaction rates leading to CFD model predictions consistent with experimentally measured reactor variables. These rate expressions should not be viewed as resolving the detailed catalyst-specific surface reaction mechanism, which is not well established for Ni on BZCY substrates. Specifically, with respect to the catalytic reaction kinetics employed in the CFD model, Xu and Froment kinetics are used, as these equations provide a general framework for modeling reforming kinetics. In addition, the Xu and Froment kinetic rate expressions involve process parameters that are fitted (in this present work, the effective catalyst weight) such that the CFD model predictions for a broad range of operating conditions are consistent with the macroscopic (input/output) reactor observables. Therefore, the employed reaction kinetics model is valid for the present experimental PMR and works well in terms of predicting reactor outputs consistent with the experimental measurements.

To employ the developed kinetic model and corresponding mole balances, a User-Defined Function (UDF) is implemented to code the thermo-electrochemical reaction rates (see Table 4). The UDF defines the consumption and production rates of each gas species as source terms in the computational grids adjacent to the anode, where all reactions are expected to occur. Specifically, the hydrogen source term is given by the stoichiometric combination of the SMR and WGS thermal reaction rates, subtracting the electrochemical hydrogen flux $\frac{I}{2F}$

Table 5
Comparison of experimental and CFD-predicted anodic hydrogen production rates.

Catalyst weight (mg)	Exp. H_2 (Nml min^{-1})	CFD H_2 (Nml min^{-1})	Error (%)
1.00	48.6	32.2	33.8
2.00	48.6	40.1	17.5
4.00	48.6	47.2	2.8
6.50	48.6	54.5	12.1
13.0	48.6	56.8	16.8

from the mole balance of hydrogen species, which represents the effect of hydrogen extraction through the protonic membrane. A uniform extraction rate is assumed across the entire anode, neglecting local variations in current density.

In the PMR, the mass of the catalyst embedded on the anode surface is unknown. To determine an appropriate effective catalyst weight, various catalyst weights were adjusted in the CFD simulations to match experimental kinetic trends. The simulation results were then compared with the experimental results to identify the best match. Specifically, the anodic and cathodic volumetric flow rates of hydrogen in the CFD simulations were compared with the experimentally equivalent measurements, and the relative errors of the model predictions for each gas species were determined. The results are summarized in Table 5. Based on these comparisons, the CFD simulation with a SMR and WGS catalyst weight of 4.0 mg showed the best agreement with experimental results.

Remark 2. To determine the effective catalyst weight for calculating the reaction source terms in each computational grid adjacent to the protonic membrane wall, homogeneous catalyst loading along the protonic membrane surface was assumed. This approximation method ensures that the local catalyst mass is distributed proportionally across the defined catalyst cells in the computational domain. The Xu and Froment intrinsic kinetic rates, originally expressed on a catalyst-mass basis (r_1 and r_2, mol kg_{cat}^{-1} s^{-1}), were converted into mass flow production source terms (R_i, kg m^{-3} s^{-1}) to ensure dimensional consistency with the species conservation equations solved in ANSYS Fluent. Each species' production or consumption rate was scaled by the local catalyst weight and normalized to the corresponding cell volume. Using this approach, the production and consumption rates of each species in catalyst cells can be accurately determined based on the local catalyst weight. The `DEFINE_EXECUTE_AT_END` macro was utilized in Fluent to determine the gas species and energy source terms at the end of each iteration step and to store these values in user-defined memory (UDM). Subsequently, the `DEFINE_SOURCE` macro was used to access the stored volumetric source terms for integration into the relevant species and energy conservation equations [21].

5.2. PMR flow field characterizations

In fluid dynamics simulations of gas flows in reactors, generally, compressibility effects become significant in high-velocity regimes. When the velocity of a fluid approaches or exceeds the local speed of sound, pressure–density coupling must be considered, as density variations strongly influence the computed velocity, pressure, and temperature distributions [22]. Flow compressibility effects are typically quantified using the Mach number (Ma), which is described as:

$$Ma = \frac{u}{c} \tag{8}$$

where c is the speed of sound in the gas flow:

$$c = \sqrt{\gamma RT} \tag{9}$$

$$\gamma = c_p / c_v \tag{10}$$

with γ representing the ratio of specific heats. Based on the PMR feed conditions listed in Table 7, the Mach number is approximately 10^{-4}, well below 0.1. This indicates that compressibility effects are negligible, and density variations due to pressure changes can be safely ignored in the model. Therefore, an incompressible flow model is used. Furthermore, a pressure-based solver is chosen over a density-based solver, given that the pressure-based solver is capable of resolving flows spanning from incompressible to moderately compressible regimes [22]. In earlier studies, we determined the optimal operating conditions for the PMR system [16]. In that work, the second Damköhler number, which compares the characteristic time scale of methane molecular diffusion with those of the SMR and WGS surface reactions, was found to be on the order of 10^{-1} for a methane feed flow rate of 16.2 Nml min^{-1}. The same methane feed flow rate is used as the initial input to the nickel feed tube. This indicates that hydrogen production reactions operate in a kinetically-controlled regime rather than being limited by mass transport under the operating conditions considered, thereby supporting the model simplification of neglecting an explicit catalyst layer representation in the CFD model.

The density for an incompressible ideal gas fluid is determined by:

$$\rho = \frac{P}{\frac{R}{M_w} T_{fluid}} \tag{11}$$

where the P is the operating pressure of the system, R is the universal gas constant, M_w is the molecular weight and T_{fluid} is the local temperature of the fluid. The operating pressure serves as a reference value for determining the gas density when using the ideal gas law in CFD simulations. For incompressible flow, density variations with pressure are neglected, and the density is calculated based on the operating pressure and temperature, which simplifies the numerical solution for low Mach number flows.

The Reynolds number is a dimensionless quantity used to characterize the bulk flow regime by relating the inertial to the viscous forces present in a control volume [23,24]. Laminar flow typically occurs for $Re < 2000$, while turbulent flow is observed for $Re > 2300$ [25]. Based on the feed conditions provided in Table 6, a Reynolds number of 7 is calculated for the flow of the bulk fluid at the feed tube inlet. This value, together with literature evaluations of high-temperature wash-coated reformers operating under laminar flow at similar conditions and geometries [26–28], supports the assumption of a laminar flow regime in the multi-physics PMR model.

In summary, the CFD model is developed based on the following assumptions:

1. The gas phase behaves as an incompressible ideal gas, with the fluid density computed from the ideal gas law under constant pressure conditions.
2. The simulations are conducted under steady-state conditions.
3. Uniform heat flux at the boundary of the protonic membrane wall throughout the axial spatial domain.
4. The catalyst is assumed to be uniformly distributed along the membrane wall, and its internal transport effects are incorporated via the effective catalyst weight used in the reaction kinetics model.
5. A Faradaic efficiency of 100% is assumed for HER/HOR, indicating that all applied current is fully utilized for driving the hydrogen extraction rate.
6. The solid material properties, including heat capacity, thermal conductivity, and density, are assumed constant.

Table 6
Fluid properties used for Reynolds number calculation.

Property	Value
Density	4.90×10^{-1} kg m^{-3}
Velocity	6.40×10^{-2} m s^{-1}
Dynamic viscosity	3.17×10^{-5} kg m^{-1} s^{-1}

5.3. Boundary conditions

The defined source terms and boundary conditions are detailed here. Key boundaries include the nickel feed tube walls, the anode chamber boundaries (anodic inlet and outlet), and the anode. The parameters applied to these boundaries are summarized in Table 7. At the inlet of the feed tube, all boundary conditions, including the mass flow rate, the composition of the gas mixture, and the reforming temperature, were set according to the experimental operating points and conditions. The anode chamber outlet was modeled as a pressure outlet, while the protonic membrane anode was assigned a constant heat flux and a non-slip condition. For the nickel feed tube, a coupled thermal boundary was applied to ensure heat flux continuity between the solid and fluid phases. Non-slip and zero species flux assumptions were also imposed at the solid feed tube interface to ensure zero velocity and zero mass flux at the feed tube boundary. The anode is another critical region where reaction and heat source terms are applied. Therefore, the thermo-electrochemical reactions are defined as source terms in the UDF, at the protonic membrane wall boundary (anode), based on the governing equations shown in Section 5.1.

The energy balance across the modeled reformer includes the enthalpy of the anodic feed, the heats of reaction for SMR and WGS, heat losses to the surroundings, and heat generation associated with electrochemical hydrogen extraction. The exact heat flux profile of the experimental PMR was not measured. Thus, to represent the combined effects of heat transfer, a constant heat flux boundary condition is applied to the anode. This approximation allows the simulation to capture the overall heating effects on the membrane walls, feed tube, and the convective fluid mixture. To ensure the validation of this heating simulation, the applied heat flux is iteratively adjusted to match the CFD-predicted temperature distribution with experimental temperature data. This approach involves comparing the temperatures in the CFD model geometry to the corresponding positions in the experimental PMR and adjusting the applied heat flux in the simulation to match observations.

Remark 3. The decision to apply a simplified heat flux boundary condition at the anode wall (anode–membrane interface), rather than explicitly modeling the cathode chamber's thermal resistance, is based on experimental and modeling practicalities. In a laboratory-scale furnace, the heat transfer involves a complex series of radiation and convection steps through intermediate gas layers. Directly measuring the local flux variations throughout these layers is experimentally infeasible. Therefore, an aggregated heat flux at the boundary was used and calibrated to match the experimental reformer outlet. Even with a more complex model, the outer furnace boundary would still require an assumed or fitted thermal profile. By applying the heat flux condition at the anode wall, a reduction in error accumulation is realized because thermocouple measures the anodic fluid temperature in experiments, not the cathodic fluid temperature. Since the system is kinetically driven, the modeling priority was to accurately reflect the thermal environment of the catalyst bed.

6. Mass, momentum and energy transport

The governing equations for conservation of mass, momentum, energy, and species transport within the 2D PMR computational domain are presented in the following subsections.

6.1. Conservation of mass in fluid regions

The continuity equation for the computational domain takes the form:

$$\frac{\partial \rho}{\partial t} + \nabla \cdot (\rho \vec{v}) = S_m \tag{12}$$

where ρ denotes the fluid density, $\vec{v}$ is the velocity vector, and S_m represents the mass exchanged to or from the gas phase through any user-defined source terms. Specifically, the term S_m (kg m^{-3} s^{-1}) represents the mass source term in the overall continuity equation and is needed to mathematically represent hydrogen flux from the defined control volume into the cathode chamber. The extraction of hydrogen from the anode chamber results in a net removal of mass from the anodic gas mixture. This physical loss is represented in the continuity equation by a nonzero total mass source term, S_m. The divergence of the velocity field, $\nabla \cdot \vec{v}$, captures volumetric flow rate changes induced by reaction-driven mass transfer.

6.2. Species transport in fluid regions

The species transport differential equations govern the mass fractions Y_i of each species i in the bulk fluid phase of the PMR, accounting for convective transport, diffusive transport, and reaction source terms. The species balances are expressed as:

$$\frac{\partial}{\partial t}(\rho Y_i) + \nabla \cdot (\rho \vec{v} Y_i) = -\nabla \cdot \vec{J}_i + R_i, \tag{13}$$

where Y_i is the mass fraction of species i, ρ is the fluid density, $\vec{v}$ is the velocity vector, $\vec{J}_i$ is the diffusive flux of species i, and R_i represents the net rate of production or consumption of species i due to chemical reactions. Chemical reactions conserve total mass, so the net loss of overall mass from the control volume due to hydrogen extraction is included in the S_m term of Eq. (12). The source terms R_i (kg m^{-3} s^{-1}) in the species mass balances, on the other hand, represent the total mass added or removed from gas species i. Please note that R_i and S_m have the same units, however, R_i represents mass generation or consumption of species i and S_m represents the total mass added to or removed from the control volume. The diffusive flux $\vec{J}_i$ of species i is modeled by Fick's law:

$$\vec{J}_i = -\rho D_{ij} \nabla Y_i, \tag{14}$$

where D_{ij} is the binary species diffusion coefficient, determined by the Chapman–Enskog formula [29] based on the Lennard-Jones parameters:

$$D_{ij} = 0.00188 \frac{T^{3/2}}{p \sigma_{ij}^2 \Omega_D} \left(\frac{1}{M_{w,i}} + \frac{1}{M_{w,j}} \right)^{1/2} \tag{15}$$

where p is the absolute pressure, M_w is the molecular weight, c_p is the heat capacity, σ is the collision diameter, and Ω is the collision integral [30].

6.3. Momentum transport in fluid regions

The Eulerian general momentum conservation equation in a non-accelerating (inertial) frame in CFD is expressed as:

$$\frac{\partial}{\partial t}(\rho \vec{v}) + \nabla \cdot (\rho \vec{v} \vec{v}) = -\nabla p + \nabla \cdot (\bar{\tau}) + \rho \vec{g} \tag{16}$$

where ρ is the fluid density, $\vec{v}$ is the velocity vector, $\bar{\tau}$ denotes the viscous second-order stress tensor, and $\vec{g}$ is the gravitational acceleration vector [31]. The term $\nabla \cdot (\rho \vec{v} \vec{v})$ represents the convective transport of momentum in a fluid, where $\vec{v}\vec{v}$ denotes a second order dyadic tensor, which is transformed into a vector by the divergence operator, accounting for the net rate of momentum flux in and out of a control volume in each direction. [32]. For incompressible flow, the stress tensor is defined as:

$$\bar{\tau} = \mu \left[\left(\nabla \vec{v} + \nabla \vec{v}^{\mathrm{T}} \right) \right] \tag{17}$$

Table 7
Boundary conditions used in the PMR model.

Position	Boundary description	Boundary condition
Anodic feed	Constant mass flow rate	$\dot{m} = 8.88 \times 10^{-7}$kg s^{-1}
	Constant gas composition	CH_4: 16.16 Nml min^{-1} H_2O: 43.05 Nml min^{-1} H_2: 9.00 Nml min^{-1} Ar: 3.49 Nml min^{-1}
	Constant inlet temperature	T = 177 °C
Anodic effluent	Zero reversed flow	$u_n \geq 0$
Protonic membrane wall	Constant heat flux	$q = q_{\text{wall}}$
	No-slip wall	$\vec{u} = \vec{0}$
Nickel feed tube	Coupled thermal boundary	$\kappa_f \frac{\partial T_f}{\partial n} = -\kappa_s \frac{\partial T_s}{\partial n}$
	No-slip wall	$\vec{u} = \vec{0}$
	Zero species flux	$\frac{\partial Y_i}{\partial n} = 0$

where μ is the dynamic viscosity of the fluid, $\nabla\vec{v}$ is the velocity gradient tensor, and $\nabla\vec{v}^{\mathrm{T}}$ is its transpose. The sum of these parameters represents the rate-of-strain tensor, which accounts for deformation due to shear forces. For incompressible flows, $\nabla \cdot \vec{v} = 0$, so the contribution from volumetric expansion or compression is neglected [33].

The viscosity for the PMR gas mixture is determined by the ideal gas mixing law based on the Wilke method [34]. Alternatively, the viscosity for each gas species is determined using the ANSYS Fluent built-in kinetic model based on the Chapman–Enskog theory [35]. The following equations describe both theories:

$$\mu_i = 2.67 \times 10^{-8} \frac{\sqrt{M_w T_{fluid}}}{\sigma^2 \Omega} \tag{18}$$

$$\mu = \sum_i \frac{X_i \mu_i}{\sum_j X_j \phi_{ij}} \tag{19}$$

$$\phi_{ij} = \frac{\left[1 + \left(\frac{\mu_i}{\mu_j}\right)^{1/2} \left(\frac{M_{w,j}}{M_{w,i}}\right)^{1/4}\right]^2}{\sqrt{8\left(1 + \frac{M_{w,i}}{M_{w,j}}\right)}} \tag{20}$$

where X_i is the mole fraction of species i, μ_i is the dynamic viscosity of species i, μ_j is the dynamic viscosity of species j, and ϕ_{ij} is the interaction parameter between species i and j, M_w is the molecular weight of species i, σ is the collision diameter, and Ω is the collision integral [36].

In general, the developed momentum equation assumes a Newtonian fluid with dynamic viscosity μ, representing the internal friction. The left-hand side captures the rate of change of momentum and convective transport, while the right-hand side includes the effects of pressure gradient, viscous diffusion, and body forces. This equation ensures that momentum is balanced throughout the entire spatial domain, taking into account both internal fluid motion and external fluid influences, such as gravity.

6.4. Energy transport in fluid regions

The general heat transport equation has the form:

$$\frac{\partial}{\partial t}\left(\rho_{\text{fluid}} E_{\text{fluid}}\right) + \nabla \cdot \left(\vec{v}\, \rho_{\text{fluid}} E_{\text{fluid}}\right) = \nabla \cdot \left(k_{\text{fluid}} \nabla T_{\text{fluid}}\right) - \nabla \cdot \left(\sum_i h_i \vec{J}_i\right) + \sum_i \Delta H_{\text{rxn,i}} + q_{\text{wall}} \tag{21}$$

where E_{fluid} is the specific total energy of the bulk fluid mixture. The first two terms on the left-hand side represent the transient change in total energy of the bulk fluid. The total energy for this fluid is separately defined as:

$$E_{\text{fluid}} = U_{\text{fluid}} + \frac{v^2}{2} \tag{22}$$

where U_{fluid} is the specific internal energy of the bulk fluid, $\frac{v^2}{2}$ is the kinetic energy due to the macroscopic motion of the bulk fluid, and U_{fluid} is calculated from the sum of the specific enthalpy and the pressure–volume work contribution:

$$U_{\text{fluid}} = H_{\text{fluid}} - \frac{P}{\rho_{\text{fluid}}} \tag{23}$$

Here, ρ_{fluid} is the fluid density. The fluid enthalpy H_{fluid} is defined as:

$$H_{\text{fluid}} = \sum_j Y_j H_j + \frac{P}{\rho} \tag{24}$$

$$h_j = \int_{T_{\text{ref}}}^{T} c_{p,j}\, dT \tag{25}$$

where Y_j is the mass fraction of species j, and h_j is the specific enthalpy of species j, calculated from the specific heat $c_{p,j}$ relative to a reference temperature T_{ref}, which is 298.15 K. The specific enthalpy of species $c_{p,j}$ is calculated using NASA polynomial expressions [37]. The mixture specific heat is then obtained by mixing law of the individual $c_{p,j}$ values:

$$c_p = \sum_i X_j\, c_{p,j} \tag{26}$$

The thermal conductivity of the bulk fluid is calculated from the ideal gas mixing law for gas mixtures:

$$k_i = \frac{15}{4} \cdot \frac{R}{M_w} \mu \left[\frac{4}{15} \cdot \frac{c_p M_w}{R} + \frac{1}{3}\right] \tag{27}$$

$$k_{fluid} = \sum_i \frac{X_i k_i}{\sum_j X_j \phi_{ij}} \tag{28}$$

$$\phi_{ij} = \frac{\left[1 + \left(\frac{\mu_i}{\mu_j}\right)^{1/2} \left(\frac{M_{w,j}}{M_{w,i}}\right)^{1/4}\right]^2}{\sqrt{8\left(1 + \frac{M_{w,i}}{M_{w,j}}\right)}} \tag{29}$$

where k_i is the thermal conductivity of species i, k_{fluid} is the thermal conductivity of the gas mixture, R is the universal gas constant, M_w is the molecular weight of species i, μ is the dynamic viscosity of species i, c_p is the specific heat capacity of relevant components at constant pressure, and ϕ_{ij} is the interaction parameter between species i and j.

The second term in the energy balance (Eq. (21)) primarily represents the convective transport of energy by the bulk fluid traveling through the PMR. The balance includes internal energy but neglects pressure-work contributions, $P\nabla \cdot \vec{v}$, which is negligible for incompressible flow. On the right-hand side, k_{fluid} and T_{fluid} are the thermal conductivity and temperature of the fluid, representing heat conduction within the fluid. The term $-\nabla \cdot \left(\sum_i h_i \vec{J}_i\right)$, where h_i is the specific enthalpy and $\vec{J}_i$ the diffusive mass flux of species i, captures enthalpy transport due to species diffusion through the bulk and toward the boundaries of each solid phase. The summation $\sum_i \Delta H_{\text{rxn},i}$ therefore

accounts for the net enthalpy change within the computed regions of the PMR unit, representing the balance between the heat absorbed by the endothermic SMR reaction and the heat released by the exothermic WGS reaction. Finally, q_{wall} represents the heat flux applied at the protonic membrane boundary. Together, these terms represent the evolution of energy transport throughout the bulk fluid of the PMR.

6.5. Energy transport in the solid region (nickel feed tube)

The energy transport within the solid nickel feed tube is governed by the transient heat conduction equation:

$$\frac{\partial(\rho_{solid} H_{solid})}{\partial t} = \nabla \cdot (k_{solid} \nabla T_{solid}) + S_s \tag{30}$$

$$H_{solid} = \int_{T_{\text{ref}}}^{T} c_{p,solid}\, dT \tag{31}$$

where ρ_{solid}, H_{solid}, k_{solid}, T_{solid}, S_s are the density, specific enthalpy, thermal conductivity, local temperature, and any volumetric heat source within the solid phase (nickel feed tube). The feed tube does not generate internal heat, so $S_s = 0$. Instead, heat is primarily transferred to the solid-phase feed tube through heat conduction driven by a temperature differential in the surrounding fluid regions. The enthalpy of the solid phase is defined in mass units in the simulation, since $c_{p,solid}$ is also in mass units. Thus, the time derivative of the solid phase enthalpy, when multiplied by density, becomes J m^{-3} s^{-1}, which are the same units of the heating source term for the reaction enthalpies in Eq (21). At the fluid–solid interface of the nickel feed tube, conjugate heat transfer (CHT) conditions are applied to ensure the continuity of temperature and heat flux, such that

$$k_{solid} \frac{\partial T_{solid}}{\partial n} = k_{fluid} \frac{\partial T_{fluid}}{\partial n} \tag{32}$$

where k_{fluid} and T_{fluid} are the thermal conductivity and temperature of the fluid at the solid interface, and $\partial/\partial n$ denotes the normal derivative at the feed tube boundaries (standard notation for boundary conditions in transport phenomena to ensure the continuity of heat flux across the interface). The feed tube enthalpy, H_{solid}, is equivalent to its internal energy since pressure effects are negligible in solids. This formulation ensures that the heat conducted through the bulk fluid is accurately transferred to the nickel feed tube.

7. CFD model results and discussion

In this section, spatially resolved contour profiles of temperature, species concentrations, density, and velocity enable evaluation of global reformer performance metrics. These metrics include reactant conversion, hydrogen product purity, heat losses, and effective fluid transport. The model was first validated under steady-state conditions through a comparison with experimental PMR data for two representative operating cases: (i) without hydrogen extraction and (ii) with hydrogen extraction through the membrane.

7.1. CFD model validation and analysis for case I: Zero hydrogen flux

The first case establishes hydrogen production rates in the absence of electrochemical hydrogen separation. As shown in Fig. 5, the average volumetric flow rates of anodic gas species predicted by the CFD model mirrored experimental observations, demonstrating the accuracy of the model at a current density of 0.0 A cm^{-2}. Moreover, the consistent trends across all species indicate that the model effectively captures both the reaction kinetics and transport processes in the PMR system. Any small deviations in predicted flow rates that are observed at lower temperatures, especially at 584 and 631 °C, can be attributed to experimental measurement uncertainties or numerical errors when species concentrations are close to zero. Overall, the close match validates the model's ability to predict steady-state anodic species concentrations over a larger range of operating temperatures. Hydrogen production

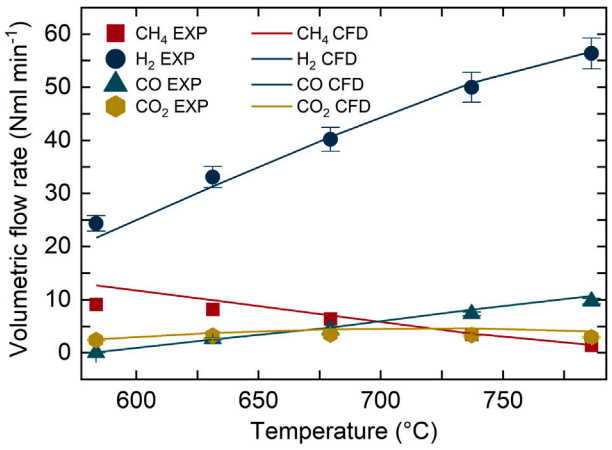

Fig. 5. Comparison of CFD calculated and experimental gas production rates at 0.0 A of applied current. Steady-state production rates at five distinct temperatures are compared with CFD steady-state simulation results. Specifically, volumetric flow rates (Nml min^{-1}) of bulk fluid components are evaluated for both datasets; water vapor is condensed prior to gas product quantification in the experimental system and is therefor excluded from the figure. Experimental data points are also presented with error bars to indicate measurement uncertainty.

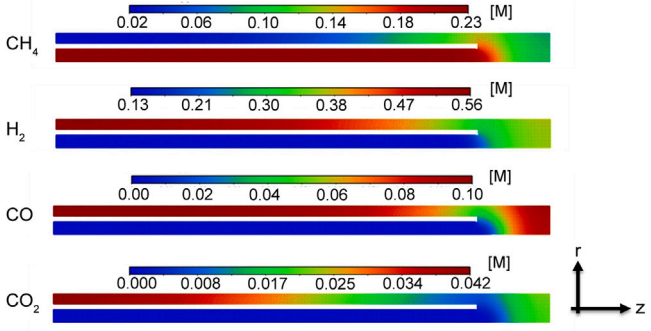

Fig. 6. Mole fraction contour plots of CH_4, H_2, CO, and CO_2 at steady-state conditions (i = 0.0 A, P = 3.2 bar, T = 786 °C).

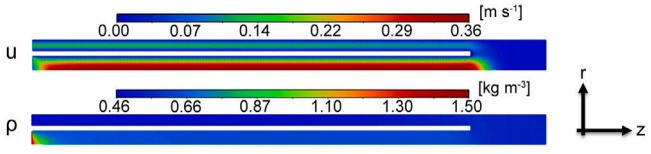

Fig. 7. Contour plots of gas velocity magnitude (u, m/s) and gas density (ρ, kg m^{-3}) at steady-state conditions (i = 0.0 A, P = 3.2 bar, T = 786 °C).

and methane consumption increase with operating temperature, as expected for kinetically-dominant operating conditions. The carbon monoxide production rate increases at higher temperatures, which is consistent with both kinetic and thermodynamic expectations. The endothermic SMR reaction and the exothermic WGS reaction exhibit opposing temperature dependencies: at higher temperatures, the SMR equilibrium shifts toward products (H_2 and CO), whereas the WGS equilibrium shifts toward reactants (CO and H_2O) [38]. The combination of accelerated carbon monoxide production via SMR, and limited carbon monoxide consumption via WGS, leads to the observed increase in the carbon monoxide molar concentration in the reacting fluid mixture.

The steady-state mole fractions for each anodic species is shown in Fig. 6. A minimum hydrogen mole fraction occurs at the inlet of the anode chamber, where hydrogen is introduced as a feed gas to

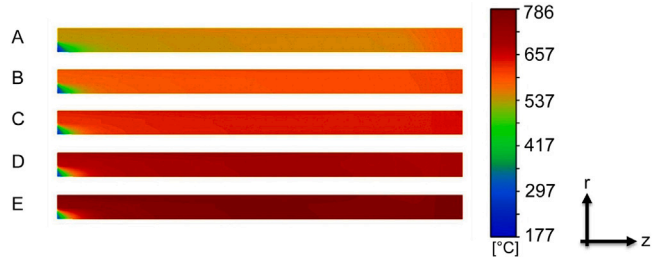

Fig. 8. Simulated temperature contour plots of the PMR at 0.0 A, 3.2 bar, and five different operating temperatures: (A) 584 °C, (B) 631 °C, (C) 679 °C, (D) 737 °C, and (E) 786 °C. In (A)-(E), the reported temperatures are reported at $z = 0.05$ m, which is the approximate position of the thermocouple in the experimental PMR unit.

limit coke-producing side reactions. Along the axial length of the anode chamber, toward the anode chamber outlet, the hydrogen mole fraction increases nonlinearly from 0.1 to 0.3 within the first 2.0 cm of the anode chamber. This significant increase in the hydrogen mole fraction suggests that the hydrogen production rate is maximized along the first 1/3 of the anode surface (Fig. 6, read from right to left). Subsequently, the hydrogen mole fraction continues to increase throughout the anode chamber as the WGS reaction approaches a maximum near the anode chamber outlet. Methane conversion is also shown in Fig. 6. The methane mole fraction is highest in the anodic feed near the anode chamber inlet. As the anodic feed comes into contact with the anode, the methane mole fraction decreases significantly, indicating rapid methane conversion along the first 1/3 of the protonic membrane reformer length. Similar trends are observed for carbon monoxide and carbon dioxide: both species are absent in the anodic feed, with their mole fractions increasing immediately as the anodic feed first reaches the anode, where reaction rates are highest. From this point, both of the carbon oxide mole fractions increase gradually along the membrane as the SMR and WGS reactions progress through the axial-length of the reformer.

Fig. 7 shows the velocities and densities of the gas mixture in the feed tube and the anode chamber of the PMR unit. The velocity profiles are dictated by temperature and the cross-sectional areas of the tube-in-tube reformer geometry; the gas velocity in the nickel feed tube is higher due to its smaller cross-sectional area. In the MEA cap region, where there is extra volume in the anode chamber, the velocity of the feed mixture drops to near-zero. Downstream, the gas velocity of the anodic effluent is lower than that of the anodic feed, but is still higher than the gas velocity in the stagnated cap region. The changes in velocity are attributed to the different diameters of the anode chamber main region, the anode chamber inlet, and the nickel feed tube. Specifically, the anode chamber outlet cross-sectional area, 0.23 cm^2, is larger than that of the anode chamber inlet, 0.08 cm^2, but smaller than that of the cap region, 0.38 cm^2. As a result, the density within the anode chamber inlet is slightly higher than in the remaining regions of the anode chamber, though the highest fluid density occurs at the feed tube inlet. This variation is primarily due to temperature gradients throughout the unit. The anodic feed at the feed tube inlet has the lowest temperature, leading to a higher gas density; the reacting fluid near the anode surface experiences the higher temperatures, causing a corresponding decrease in the density of the reacting gas mixture adjacent to the anode.

The temperature predictions of the CFD simulation elucidate the axial and radial temperature profiles that are not measurable in the experiment, which highlights the importance of this multi-physics model. Fig. 8, in particular, presents temperature contour plots for five anode chamber outlet temperatures: 584, 631, 679, 737, and 786 °C. For all outlet conditions, the temperature of the feed tube inlet is lowest, caused by the entry of cool feed gas into the PMR unit. The temperature maxima are located at two points, namely, the anode surface and the MEA cap region. The anode surface is closest to the specified heat source and the gas stagnation layer in the cap region leads to locally higher temperatures. In Fig. 9, the 1D axial profiles of the temperature of the anode chamber and the molar concentrations of gas species provide further insight into the performance of the reformer at the anode. In Fig. 9(a), the reformer temperature begins to decrease at $z = 0.05$ m, as energy is consumed by the highly endothermic SMR reaction. Along the anode chamber toward the outlet (from $z = 0.05$ m to $z = 0.02$ m), the temperature gradually increases as the SMR reaction rate decreases, consistent with our conclusion for the steady-state mole fraction contour plots (Fig. 6).

According to the molar concentration profiles in Fig. 9(b), the molar concentration of hydrogen, carbon dioxide, and carbon monoxide increases, while those of methane and water decrease at $z = 0.05$ m. From $z = 0.05$ m to $z = 0.00$ m, the concentrations of hydrogen and carbon oxides increase while the methane concentration decreases, consistent with the progression of the SMR and WGS reactions along the axial length of the reformer. This trend reflects the approach toward reaction equilibrium and indicates continuous reaction activity along the anode surface. Additionally, the location where these concentration changes occur aligns with the point of temperature reduction in Fig. 9(a), demonstrating that the highest hydrogen production rate occurs at approximately $z = 0.05$ m, corresponding to the initial region of the catalyst. A similar species trend was observed in the study by [8], where species consumption was highest at the PMR inlet and gradually decreased in the axial direction toward the PMR outlet.

7.2. CFD model validation and analysis for case II: Non-zero hydrogen flux

After validating the CFD model for the first case (zero hydrogen flux), a non-zero hydrogen flux was introduced to systematically evaluate rates of hydrogen extraction on the performance of the PMR unit. The comparison between CFD simulation results and experimental results under steady-state conditions for hydrogen extraction currents of 4.5 A (0.30 A cm^{-2}) and 9.0 A (0.59 A cm^{-2}) are presented in Fig. 10. The figure compares the average outlet volumetric flow rates of anodic effluent species, as well as cathodic hydrogen, predicted at 786 °C and 3.2 bar, with experimental measurements obtained under the same conditions. As shown in Fig. 10(a), when 4.5 A of current is applied, the deviations between the CFD predictions and the experimental results are generally low for the anode chamber outlet composition. For the anodic carbon dioxide, cathodic hydrogen, and anodic hydrogen volumetric flow rates, the CFD predictions fall within the experimental error bars. These deviations are acceptable, as most of the species remain within or slightly outside the experimental error bars. Specifically, the relative error for CFD predicted anode and cathode hydrogen production flow rates are 11.1% and 0.95%, respectively, which are reasonable considering uncertainties in experimental measurements, fluctuations in sensor readings, and potential discrepancies between the catalyst weight used in the experiment and the effective catalyst weight in the CFD model.

In Fig. 10(b), when a current density of 0.59 A cm^{-2} is applied to the PMR unit, the CFD model prediction for extracted hydrogen has a relative error of 6.6%. The CFD-predicted total hydrogen production rate, defined as the sum of anodic and cathodic hydrogen flow rates (67.6 Nml min^{-1}), has a relative error of 3.3%. Thus, the overall reaction kinetics are well-captured, while the minor deviations in individual chamber flow rates indicate a slight over-estimation of the hydrogen flux from the anode to the cathode chamber that is still within the experimental measurement error. The over-estimation of hydrogen flux is expected, given the assumed Faradaic efficiency of 100% for all current densities in the CFD model. In fact, experimental measurements achieved 93% Faradaic efficiency at current densities at or above 0.59 A cm^{-2}. While CFD-predicted cathodic hydrogen flow rates are slightly higher than experimental values at current densities

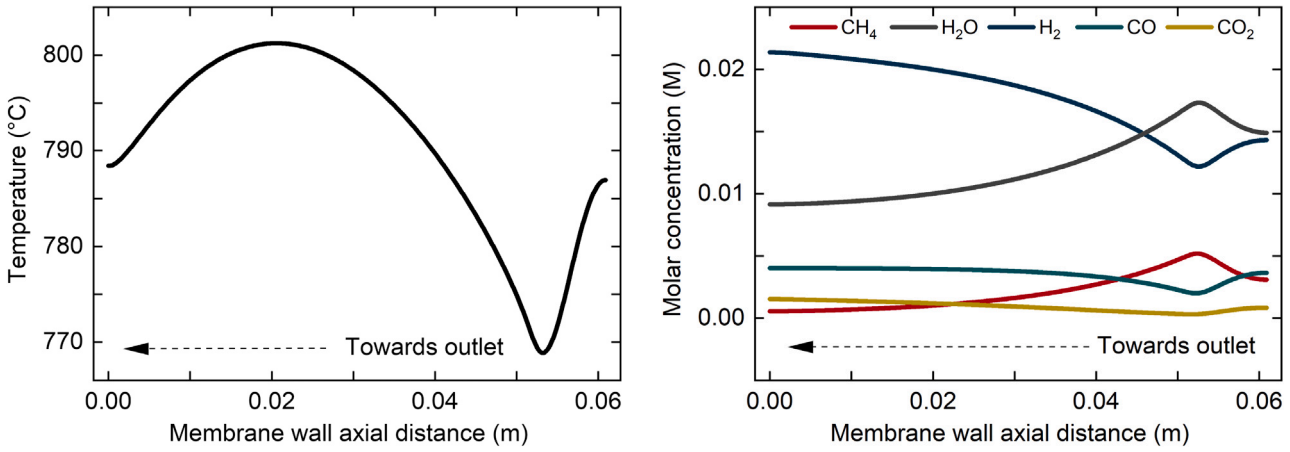

(a) PMR temperature profile.

(b) Concentration profiles of gas species.

Fig. 9. Modeled 1D axial gas species concentrations and temperature profiles along PMR reaction zone at 0.0 A of applied current. In the axial direction, $z = 0.00$ m corresponds to the catalyst surface near the reactor outlet, and $z = 6.10 \times 10^{-2}$ m corresponds to the anode surface closest to the MEA cap.

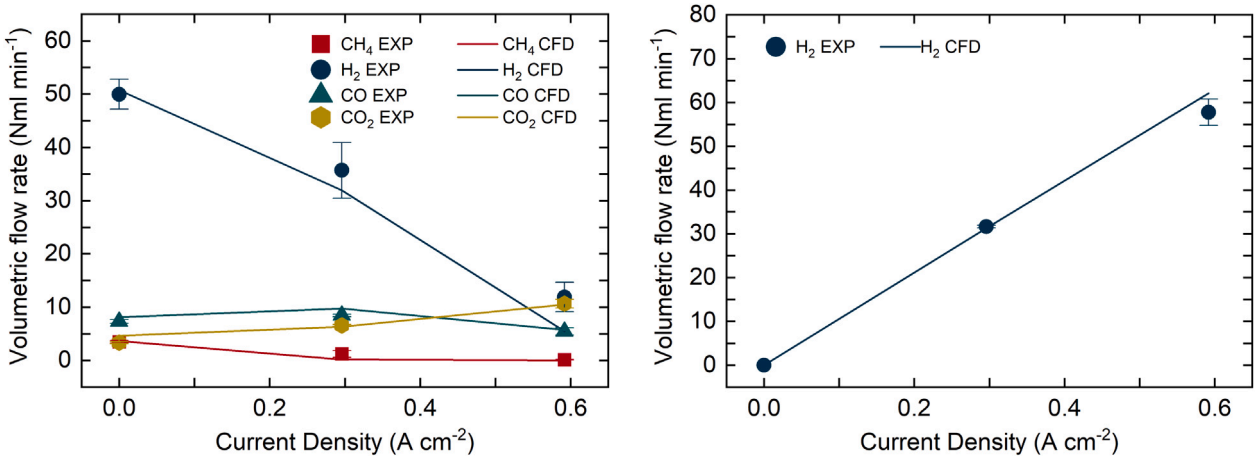

(a) Anodic product distributions at multiple current densities.

(b) Cathodic hydrogen extraction rates at multiple current densities.

Fig. 10. Comparison of CFD calculated and experimental volumetric flow rates (Nml min^{-1}) of hydrogen (in both the anode and cathode chambers), and anodic species, at 4.5 A (0.30 A cm^{-2}) and 9.0 A (0.59 A cm^{-2}) of applied current. Both datasets correspond to steady-state conditions under an operating pressure of 3.2 bar and a temperature of 786 °C. The cathodic hydrogen flow represents the amount of hydrogen extracted when the hydrogen flux is non-zero. Water is condensed prior to gas product quantification in the experimental system and is therefore excluded from the figure. Experimental data are also presented with error bars to indicate measurement uncertainty.

Table 8
CFD model performance under different operating currents.

Current (A)	H_2 Prod. (Nml min^{-1})	CH_4 Conv. (%)	H_2 Recovery (%)	CO_2:CO Ratio
2.5	61.4	98.2	28.1	0.49
4.5	63.0	99.1	49.3	0.64
6.5	64.7	99.7	69.4	0.91
9.0	67.6	100	91.9	1.83

near 0.59 A cm^{-2}, the assumption of 100% Faradaic efficiency remains a reasonable approximation in the present simulations for most current densities throughout the PMR operating domain.

In Fig. 11(a), the molar concentrations of gas species along the anode chamber in the 1D axial direction are shown for the case in which the hydrogen flux through the protonic membrane is non-zero (i.e, an external fixed current at 4.5 A and 9.0 A is applied to the electrochemical circuit). Compared to the 1D axial species concentration profiles without hydrogen extraction in Fig. 9(b), the molar concentration distribution of products shows a similar trend: methane decreases as the primary reactant, while the concentrations of the carbon oxides increase. The main difference between the case studies lies in the hydrogen concentration profile along the axial length of the anode chamber; and it should be noted that hydrogen extraction at 4.5 A also separates 31.3 NmL min^{-1} of fluid volume from the anode chamber, which shifts the volume basis used to calculate species molar concentrations. When the hydrogen flux is zero, the hydrogen concentration increases monotonically along the anode surface and reaches 2.14×10^{-2} M in the anodic effluent gas mixture. By contrast, in Fig. 11(a), with hydrogen flux enabled, the hydrogen concentration

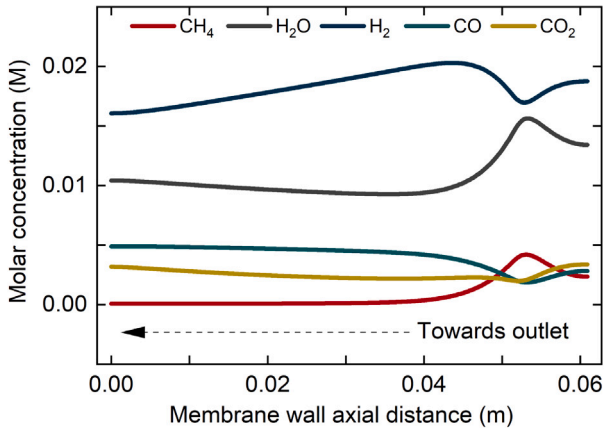

(a) 1D axial molar concentration (C, M) profiles of key gas species along the anode surface in the PMR unit at 4.5 A of applied current.

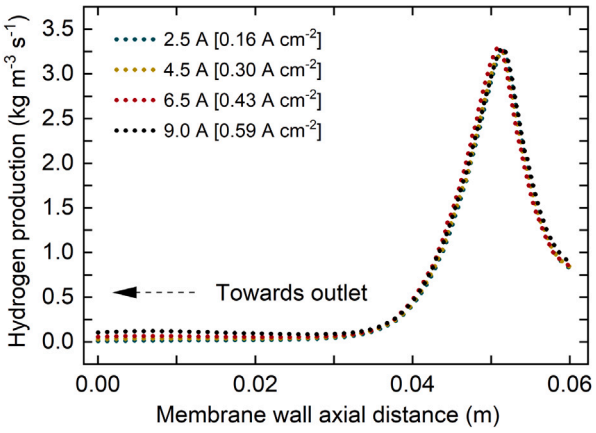

(b) 1D axial anodic hydrogen production rate (r_{H_2}, kg m^{-3} s^{-1}) distribution under four applied currents (2.5, 4.5, 6.5, and 9.0 A).

Fig. 11. Axial profiles along the anode chamber in the PMR unit. The horizontal axis represents the distance from the anode chamber outlet (z = 0.00 m) to the MEA cap ($z = 6.10 \times 10^{-2}$ m), corresponding to the anode chamber inlet.

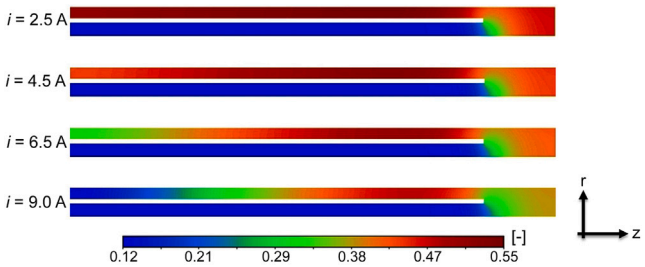

(a) Hydrogen (anodic) mole fraction contours in the anode chamber at applied currents of 2.5, 4.5, 6.5, and 9.0 A (P = 3.2 bar, T = 786 °C).

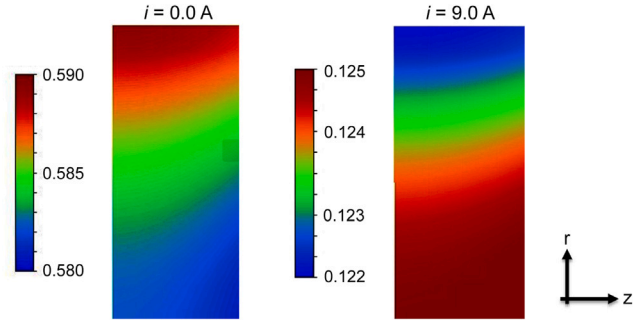

(b) Hydrogen (anodic) mole fraction contours at the anode chamber outlet at 0.0 A and 9.0 A of applied current.

Fig. 12. Hydrogen mole fraction contour profiles in the anode chamber and at the anode chamber outlet of the PMR unit. The anode chamber outlet section shown corresponds to z = [0.00 m, 6.00×10^{-4} m] and r = [2.25×10^{-3} m, 3.50×10^{-3} m]. In the outlet comparison, the left profile shows the anodic hydrogen mole fraction without extraction, while the right profile shows the anodic hydrogen mole fraction when the reformer is subject to an applied current of 9.0 A.

decreases along the axial direction of the anode chamber and hits 1.60×10^{-2} M at the anode chamber outlet, reflecting the extraction of hydrogen through the protonic membrane. The removal of hydrogen through the membrane also impacts the concentrations of other species at the anodic chamber outlet: the concentration of methane decreases from 3.8×10^{-4} M to 7.8×10^{-5} M, while the carbon monoxide and carbon dioxide concentrations increase from 4.0×10^{-3} M and 1.5×10^{-3} M to 4.9×10^{-3} M and 3.2×10^{-3} M, respectively. The shift in the thermodynamic equilibrium toward increased methane consumption and carbon dioxide production upon hydrogen removal is consistent with Le Chatelier's principle [39], validating the model's capacity to capture a different process behavior when hydrogen extraction is implemented. Larger hydrogen yields are also reflected in higher carbon dioxide production rates at 0.59 A cm^{-2} in Fig. 10(a). Overall, the species concentration profiles confirm the expected impact of hydrogen extraction on the distribution of reactants and products and shows a net gain of 16.8 NmL min^{-1} in overall hydrogen production rate (anodic plus cathodic).

When hydrogen is extracted through the protonic membrane, the local hydrogen concentration at the anode surface decreases. This phenomenon is captured in Fig. 11(b), which presents the 1D axial hydrogen production rate profile along the membrane at four distinct current densities. At all four current densities, the maximum reaction rate is observed at approximately z = 0.05 m, and gradually decreases moving away toward the outlet and the cap region, which is consistent with the previously discussed reaction phenomena. Along the axial positions of 0.03 m to 0.06 m, the hydrogen production rate is approximately the same, with a maximum value around 3.3 kg m^{-3} s^{-1}. However, from the region from 0.00 to 0.03 m, the hydrogen production rate gradually increases from 0.01 to 0.12 kg m^{-3} s^{-1} as the current applied to extract hydrogen increases from 2.5 A to 9.0 A, clearly demonstrating an increase in hydrogen production rate. Near the MEA cap region (around z = 0.05 to z = 0.06 m), the hydrogen production rate is relatively lower. This may be due to gas flow stagnation and limited convective transport, which could reduce the availability of reactants on the anode surface despite a lower local hydrogen concentration. Fig. 12(a) presents both axial and radial hydrogen mole fraction contours at applied currents of 2.5, 4.5, 6.5, and 9.0 A. Along the protonic membrane and toward the anode chamber outlet, the hydrogen mole fraction decreases from approximately 0.55 to 0.12 as the current increases from 2.5 to 9.0 A, demonstrating the removal of hydrogen from the anode chamber and to the cathode chamber in the CFD model. This is consistent with Fig. 11(b), as higher operating currents drive higher hydrogen extraction rates, leading to a depletion of the local hydrogen concentration.

To further examine the radial contribution throughout the anode chamber and near the anode surface, Fig. 12(b) presents an expanded view of the molar fraction profile of hydrogen in the anodic effluent at

0.0 A and 9.0 A of hydrogen extraction. In this region of the reformer, the hydrogen mole fraction at the anode chamber outlet decreases from 0.56 to 0.12 when the applied current to the PMR is increased from 0.0 A to 9.0 A. Despite the radial gradient induced by hydrogen extraction at 9.0 A in the CFD simulation, the variation in hydrogen mole fraction across the reformer radius remains relatively small. Being a highly diffusive gas, hydrogen rapidly diffuses from the bulk to the membrane surface, minimizing concentration differences across the radial dimension, generally. Further, in (Fig. 12(b), left), minor axial and radial hydrogen mole fraction gradients are observed. However, when hydrogen extraction is applied at 9.0 A (Fig. 12(b), right), the mole fraction gradient reverses, and the local hydrogen concentration is lower near the anode surface. As a result, a slight gradient in the hydrogen mole fraction is observed for the non-zero hydrogen flux case that ranges from 0.13 to 0.12 from $r = 2.25 \times 10^{-3}$ m to $r = 3.50 \times 10^{-3}$ m. This reversal occurs because the hydrogen extraction rate is sufficiently large to deplete the anode surface of local hydrogen molecules, indicating a net flux of hydrogen toward the membrane and into the cathode side of the electrochemical cell. Complete depletion of hydrogen on the anode surface, however, causes voltage spikes as hydrogen recovery through the membrane becomes mass transport limited. In fact, [16] recorded voltage spikes at an applied current density of 0.67 A cm^{-2}. Concurrent temperature spikes were also observed alongside voltage spikes in numerous experiments [17].

Table 8 summarizes the CFD-based hydrogen extraction simulations performed at the same temperature and pressure (786 °C and 3.2 bar) under different applied currents. The results highlight the effect of hydrogen removal on the total hydrogen volumetric flow rate (anodic plus cathodic), methane conversion, hydrogen recovery rate, and the CO_2:CO ratio. As the applied current increases from 2.5 to 9.0 A, the total hydrogen flow rate rises from 61.4 to 67.6 Nml min^{-1}, the methane conversion improves from 98.2% to 99.9%, the hydrogen recovery rate increases from 28.1% to 91.9%, and the CO_2:CO ratio increases from 0.49 to 1.83. The observed trends can be attributed to the larger driving force for hydrogen flux across the protonic membrane at higher applied currents, which increases hydrogen extraction rates. Simultaneously, increased hydrogen extraction enhances the water-gas shift reaction, resulting in a higher CO_2:CO ratio. Overall, these predictions demonstrate that protonic membrane reforming improves equilibrium-limited reforming reactions, enabling higher conversion efficiency and improved selectivity for carbon dioxide in these hydrogen production systems.

8. CFD guided strategies for future reactor optimization

The developed CFD models provide insights into the influence of operating conditions and reactor geometry on reactor performance, which can guide experimental optimization. Through parametric studies, the effects of key operating parameters, such as temperature, pressure, gas flow rates, and electric current applied to extract hydrogen, on temperature distribution, species concentration profiles, and hydrogen production rates can be systematically evaluated. These analyses can help identify the conditions that maximize reaction rates. In addition, geometric modifications, such as reducing the headspace near the cap region, can be investigated to assess their impact on fluid flow behavior, mass transport, and reaction kinetics in the initial reaction zone. Such simulations allow us to predict how these changes influence overall reactor efficiency. Although these optimizations have not yet been included in the present study, the CFD model provides a systematic framework to guide future experimental designs by prioritizing the most promising operating conditions and geometric configurations, thereby reducing experimental costs and accelerating reactor development.

Carbon formation in hydrogen-depleted regions of the PMR anode warrants further investigation, and CFD with carbon formation kinetics would be a useful research direction. Experimentally, the protonic membrane was evaluated over multiple experimental runs corresponding to a cumulative time-on-stream of 9.05 days under combined thermo-electrochemical conditions. Minimal carbon deposition was observed in the condenser section immediately downstream of the PMR anode chamber, suggesting that carbon formation within the system is limited under the operating conditions studied. Across this operating period, no measurable shift in CO:CO_2 selectivity was observed, indicating stable catalytic performance. In addition, the electrochemical performance of the membrane remained stable (FE ≈ 100%), and complete methane conversion was consistently achieved at an applied current of 9.0 A throughout the experiments. While these results indicate stable operation over the tested time-on-stream, the duration of laboratory-scale studies remains limited relative to industrial timescales. In particular, coke formation kinetics should be incorporated within detailed CFD models to rigorously assess long-term membrane stability and carbon deposition behavior under extended operation.

9. Conclusion

In this study, a 2D axisymmetric CFD model was developed and used to investigate the steady-state spatial distributions of mass and energy in a PMR unit. The model employed a lumped-parameter approach, incorporating the effects of anode surface kinetics and boundary conditions through effective physical parameters. This allowed the CFD model to replicate experimental observables without resolving a fully detailed microstructural mesh. The model also elucidates unmeasured observables like flow stagnation, radial methane diffusion, axial anodic and cathodic hydrogen compositions, and the steady-state temperature profiles throughout the feed tube and anode chamber control volumes. With the model validated against the experimental observables, a parametric study was conducted to analyze the impact of hydrogen extraction from the anode chamber on methane conversion and anodic compositional profiles. At higher applied currents (9.0 A or 0.59 A cm^{-2}), hydrogen removal was found to enhance net reaction rates, resulting in methane conversions exceeding (99.9%), higher hydrogen production rates (67.6 Nml min^{-1}), and an increased ratio of carbon dioxide to carbon monoxide (1.80:1.00) in the anodic effluent. Beyond validation, the model provides critical internal insights that can guide experimental reactor design, for tube-in-tube PMR reactor geometries, and operational optimization. For example, simulations suggest that excess space in the capped region may promote gas accumulation, which could reduce reactant transport, slow local gas flow, and decrease the overall rate of hydrogen production. This observation indicates that minimizing any unnecessary volume in the MEA cap region of the reformer might improve the reaction efficiency. Overall, the study demonstrates how CFD modeling can complement experiments by identifying design improvements that optimize reactor performance, and highlights directions for future work that focus on refining the reformer geometry and validating these design hypotheses for novel heat integration techniques.

CRediT authorship contribution statement

Yifei Wang: Writing – original draft, Methodology, Investigation, Formal analysis, Conceptualization. **Dominic Peters:** Writing – original draft, Methodology, Investigation, Formal analysis, Conceptualization. **Xiaodong Cui:** Methodology, Investigation. **Henrik Wang:** Investigation. **Feiyang Ou:** Investigation. **Carlos G. Morales-Guio:** Writing – review & editing, Supervision, Methodology, Investigation, Conceptualization. **Panagiotis D. Christofides:** Writing – review & editing, Supervision, Methodology, Investigation, Conceptualization.

Declaration of competing interest

The authors declare that they have no known competing financial interests or personal relationships that could have appeared to influence the work reported in this paper.

Acknowledgments

The authors gratefully acknowledge financial support from the U.S. Department of Energy, through the Office of Energy Efficiency and Renewable Energy (EERE), under the Advanced Manufacturing Office Award Number DE-EE0007613. The authors also express sincere gratitude to CoorsTek, Inc., for providing the BZCY proton-conducting membranes used to construct the protonic membrane reformer unit.

References

[1] Zhang L, Jia C, Bai F, Wang W, An S, Zhao K, Li Z, Li J, Sun H. A comprehensive review of the promising clean energy carrier: Hydrogen production, transportation, storage, and utilization (HPTSU) technologies. Fuel 2024;355:129455.
[2] Green Jr. L. An ammonia energy vector for the hydrogen economy. Int J Hydrog Energy 1982;7:355–9.
[3] Shen J, Zhang Q, Tian S, Li X, Liu J, Tian J. The role of hydrogen in iron and steel production: Development trends, decarbonization potentials, and economic impacts. Int J Hydrog Energy 2024;92:1409–22.
[4] International Energy Agency. Global hydrogen review 2023. 2023, URL: https://www.iea.org/reports/global-hydrogen-review-2023, IEA, Paris. Licence: CC BY 4.0.
[5] Çıtmacı B, Cui X, Abdullah F, Richard D, Peters D, Wang Y, Hsu E, Chheda P, Morales-Guio CG, Christofides PD. Model predictive control of an electrically-heated steam methane reformer. Digit Chem Eng 2024;10:100138.
[6] Sweeney DM, Alves V, Sakhai S, Dinh S, Lima FV. Techno-economic analysis and optimization of intensified, large-scale hydrogen production with membrane reactors. Ind Eng Chem Res 2023;62:19740–51.
[7] Al-Mufachi N, Rees N, Steinberger-Wilkens R. Hydrogen selective membranes: A review of palladium-based dense metal membranes. Renew Sustain Energy Rev 2015;47:540–51.
[8] Malerød-Fjeld H, Clark D, Yuste-Tirados I, Zanón R, Catalán-Martinez D, Beeaff D, Morejudo SH, Vestre PK, Norby T, Haugsrud R, et al. Thermo-electrochemical production of compressed hydrogen from methane with near-zero energy loss. Nat Energy 2017;2:923–31.
[9] Zhai X, Ding S, Cheng Y, Jin Y, Cheng Y. CFD simulation with detailed chemistry of steam reforming of methane for hydrogen production in an integrated micro-reactor. Int J Hydrog Energy 2010;35:5383–92.
[10] Ullah KS, Omer A, Rashid K, Rehman NU, Rahimipetroudi I, Kim SD, Dong SK. Modeling and comprehensive analysis of hydrogen production in a newly designed steam methane reformer with membrane system. Comput Chem Eng 2023;175:108278.
[11] Habibzadeh M, Avargani VM, Zendehboudi S. Performance assessment of a novel porous catalytic reactor with a hydrogen-selective membrane for enhanced methane dry reforming process–CFD investigation. Int J Hydrog Energy 2024;64:870–88.
[12] Kassi AH, Al-Hattab TA. A CFD model of natural gas steam reforming in a catalytic membrane reactor: Effect of various operating parameters on the performance of CMR. Int J Hydrog Energy 2024;56:780–96.
[13] Choi H, Kim SH, Bae J, Katikaneni SP, Jamal A, Harale A, Paglieri SN, Lee JH. CFD analysis and scale up of a baffled membrane reactor for hydrogen production by steam methane reforming. Comput Chem Eng 2022;165:107912.
[14] Ben-Mansour R, Haque MA, Harale A, Paglieri SN, Alrashed FS, Shakeel MR, Mokheimer EM, Habib MA. Comprehensive parametric investigation of methane reforming and hydrogen separation using a CFD model. Energy Convers Manage 2021;249:114838.
[15] Al Naji HH, Siddiqui O, Paglieri SN, Alahmed A. Multi-physics open-source computational modeling of a protonic membrane reformer for lower-carbon compressed hydrogen production. Int J Hydrog Energy 2025;103:951–63.
[16] Peters D, Cui X, Wang Y, Donahue CG, Stanley J, Morales-Guio CG, Christofides PD. Automation and control of an experimental protonic membrane steam methane reforming system. Digit Chem Eng 2025;15:100237.
[17] Peters D, Cui X, Wang Y, Morales-Guio CG, Christofides PD. Model predictive control of an experimental protonic membrane steam methane reforming system. AIChE J 2025;72:e70105.
[18] Cui X, Peters D, Wang Y, Çıtmacı B, Richard D, Morales-Guio CG, Christofides PD. Modeling and control of a protonic membrane steam methane reformer. Chem Eng Res Des 2024;212:493–519.
[19] Lao L, Aguirre A, Tran A, Wu Z, Durand H, Christofides PD. CFD modeling and control of a steam methane reforming reactor. Chem Eng Sci 2016;148:78–92.
[20] Xu J, Froment GF. Methane steam reforming, methanation and water-gas shift: I. Intrinsic kinetics. AIChE J 1989;35:88–96.
[21] Manual U. ANSYS FLUENT 12.0. Theory Guid 2009;67.
[22] Fluent. Ansys fluent theory guide. Ansys Inc., USA 2011;15317:724–46.
[23] Smith Jr. L. Some comments on Reynolds number. 1964.
[24] Uruba V. Reynolds number in laminar flows and in turbulence. In: AIP conference proceedings. 2118, (1):AIP Publishing LLC; 2019, 020003.
[25] Hillebrandt W, Kupka F. An introduction to turbulence. In: Interdisciplinary aspects of turbulence. Springer; 2008, p. 1–20.
[26] Stutz M, Poulikakos D. Optimization of methane reforming in a microreactor—effects of catalyst loading and geometry. Chem Eng Sci 2006;61:4890–903.
[27] Balzarotti R, et al. Recent advances in the development of highly conductive structured catalysts for steam methane reforming. Front Chem Eng 2022;3:811439. http://dx.doi.org/10.3389/fceng.2021.811439.
[28] Chen J, et al. Optimization of catalyst porosity and reactor design for hydrogen production in a microchannel reforming reactor. Front Energy Res 2023;11:1177623. http://dx.doi.org/10.3389/fenrg.2023.1177623.
[29] McGee HA. Molecular engineering. New York: McGraw-Hill; 1991.
[30] ANSYS. ANSYS FLUENT 12.0 user's guide. 2009, URL: https://www.afs.enea.it/project/neptunius/docs/fluent/html/ug/node776.htm, Section 1.2.3.4: Which model should I use?.
[31] Batchelor GK. An introduction to fluid dynamics. Cambridge University Press; 2000.
[32] Cohen IM, Kundu PK. Fluid mechanics. Elsevier; 2004.
[33] BSL R. Byron bird & warren e. Stewart & edwin n. Lightfoot. Transp Phenom 2002.
[34] Wilke CR. A viscosity equation for gas mixtures. J Chem Phys 1950;18(4):517–9.
[35] Chapman S, Cowling T. The mathematical theory of non-uniform gases, cambridge univ. Press, Camb Engl 1970;12(22):119.
[36] Hirschfelder JO, Curtiss CF, Bird RB. Molecular theory of gases and fluids. Wiley, New York; 1954.
[37] Chase MW, et al. NIST-JANAF thermochemical tables. J Phys Chem Ref Data 1998;28:1951.
[38] Chen W-H, Lin M-R, Jiang TL, Chen M-H. Modeling and simulation of hydrogen generation from high-temperature and low-temperature water gas shift reactions. Int J Hydrog Energy 2008;33(22):6644–56.
[39] Le Chatelier H. Recherches expérimentales et théoriques sur les équilibres chimiques. Dunod; 1888.